Magnetic Resonance in Medicine 54:645–655 (2005)

Variable-Density One-Shot Fourier Velocity Encoding

Julie C. DiCarlo,[1*] Brian A. Hargreaves,[1] Krishna S. Nayak,[2] Bob S. Hu,[1,3] John M. Pauly,[1] and Dwight G. Nishimura[1]

In areas of highly pulsatile and turbulent flow, real-time imaging with high temporal, spatial, and velocity resolution is essential. The use of 1D Fourier velocity encoding (FVE) was previously demonstrated for velocity measurement in real time, with fewer effects resulting from off-resonance. The application of variable-density sampling is proposed to improve velocity measurement without a significant increase in readout time or the addition of aliasing artifacts. Two sequence comparisons are presented to improve velocity resolution or increase the velocity field of view (FOV) to unambiguously measure velocities up to 5 m/s without aliasing. The results from a tube flow phantom, a stenosis phantom, and healthy volunteers are presented, along with a comparison of measurements using Doppler ultrasound (US). The studies confirm that variable-density acquisition of k_z-k_v space improves the velocity resolution and FOV of such data, with the greatest impact on the improvement of FOV to include velocities in stenotic ranges. Magn Reson Med 54: 645–655, 2005. © 2005 Wiley-Liss, Inc.

Key words: Fourier velocity encoding; variable-density sampling; quantitative flow imaging; magnetic resonance imaging; peak velocity

Quantitative velocity measurements are widely used in the diagnosis of cardiovascular disease. In mitral and aortic valves, the presence of a stronger peak velocity pressure gradient can indicate the degree of stenosis (1–3). Pulmonary hypertension can be detected by the presence of tricuspid regurgitation jets. In the ascending aorta, velocity pressure gradients can be used to diagnose coarctation. Doppler ultrasound (US) has the ability to measure normal and jet velocities with high temporal resolution. However, the technique is sensitive to transducer positioning and the angle of insonation (4,5). Mitigation of errors in Doppler US peak velocity measurement continues to be an active area of research (6). The development of high-resolution imaging sequences to depict coronary vessel structure (7) and measure cardiac function (8) demonstrates that MR is a compelling modality for obtaining clinically useful information that is beyond the capabilities of US. The addition of a tool that is the MR equivalent of Doppler US would complete the package of a comprehensive cardiac evaluation tool and revolutionize patient examination and monitoring.

Phase contrast, which uses bipolar gradients between slice excitation and readout, can be used to measure velocity in any direction and has been applied to jet velocity measurement (9–19). Bipolar lobes are designed to have a first moment that produces 180° of phase on a spin that is moving at the estimated maximum velocity in the sample, v_{enc}. Phase in each voxel is then mapped to a scale between zero and v_{enc}, at a resolution that depends on the size of v_{enc}. If there are multiple velocities in a single voxel, the voxel phase will be the complex-average phase of all moving spins in the voxel. This velocity averaging, which is known as partial volume averaging, can result in the underestimation of velocities in voxels containing stationary and varying-velocity spins, and, depending on the resolution parameters used, can greatly affect the maximum velocity detected.

Fourier velocity encoding (FVE) resolves the velocity spectrum and does not suffer from partial volume errors (20). Since data are acquired during a train of bipolar gradient lobes, each voxel contributes a signal with continually accruing phase during readout. The readout is similar to a sequence of phase-contrast lobes, which produce increasing encoded velocity at the same location as a function of time. This results in the acquisition of samples in 2D spatial-velocity k-space (k_z-k_v) that can be reconstructed to produce a velocity spectrum at each voxel. If enough bipolar lobes are used in the pulse train, then the velocity k-space, k_v, will be sampled adequately in addition to the spatial frequency, or k_z.

FVE can detect anomalous jet velocities more accurately than phase contrast (21,22). However, if velocity spectra are acquired in each direction, data sets are large and imaging times are too long to be clinically feasible. Imaging can instead be restricted to a single direction by the use of a 2D excitation pulse (23,24) aligned along the maximum velocity direction. When followed by the use of an FVE readout gradient on this axis, the number of k-space samples needed for reconstruction to a 2D velocity data set is reduced. This greatly reduces imaging time, making Doppler MR sequences feasible (25–29). In this paper we show that variable-density sampling of velocity k-space further reduces imaging time (30) and makes it possible to measure the real-time jet velocity (31).

We present a variable-density version of the single-shot FVE described previously by Pat et al. (29). Velocity-detection sequences with higher velocity resolution for a given readout time and velocity field of view (FOV) are presented. Variable-density sampling to produce a higher-velocity FOV while maintaining readout time and velocity resolution is then used to demonstrate unaliased images of velocities of up to 5 m/s. We present comparisons of vari-

[1]Department of Electrical Engineering, Stanford University, Stanford, California, USA.

[2]Department of Electrical Engineering, University of Southern California, Los Angeles, California, USA.

[3]Department of Cardiology, Palo Alto Medical Foundation, Palo Alto, California, USA.

*Correspondence to: Julie C. DiCarlo, Information Systems Lab, Packard EE Building, Room 210, Stanford, CA 94305-9510. E-mail: julie@mrsrl.stanford.edu

Grant sponsor: NIH; Grant numbers: R01 HL074332; R01 HL067161; Grant sponsors: NIH/NHLBI; Grant sponsor: GE Medical Systems.

Received 26 October 2004; revised 9 March 2005; accepted 30 March 2005.

DOI 10.1002/mrm.20594

Published online 8 August 2005 in Wiley InterScience (www.interscience.wiley.com).

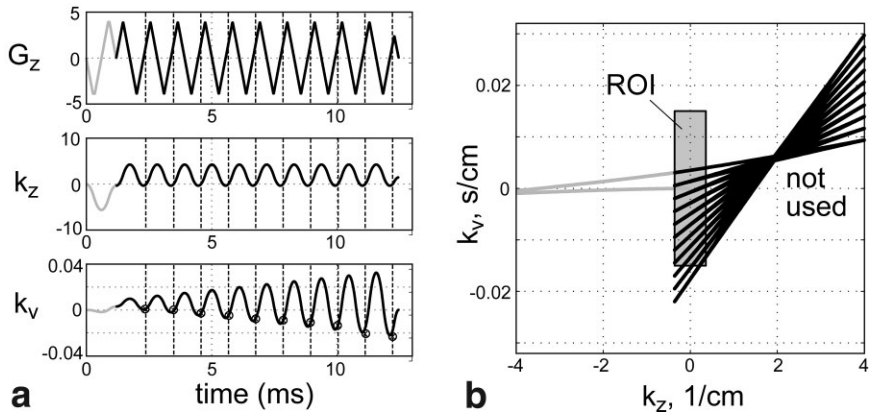

FIG. 1. **a:** Readout gradient waveform, and the resultant k_z and k_v values from the zeroth and first moments, respectively. Dashed lines mark the time samples when $k_z = 0$, or the trajectory passes through the k_v axis, during the left–right spokes in the trajectory. Marked points along these lines in the plot of k_v are used to illustrate the magnitude-increasing first moment with each successive bipolar lobe in the pulse train. **b:** Resultant velocity-position *k*-space trajectory when k_v is plotted as a function of k_z. The gray part of the waveform and trajectory represents the prewinding bipolar lobe played out before the readout gradient in order to shift the bowtie trajectory about the *k*-space origin. The gray box represents the ROI of useful data passed to the reconstruction.

able- and uniform-density FVE with Doppler US both in a flow phantom and in vivo.

THEORY

Velocity *k*-Space

When imaging is limited to one dimension by a 2D excitation pulse, an oscillating gradient can be used to sample velocity-position *k*-space, or k_v-k_z. The oscillating gradient serves as a series of bipolar pulses applied in succession. As the gradient is played, the spins in voxels along the length of the excitation experience larger and larger gradient first moments as the trajectory moves back and forth in k_z. This forms a bowtie-shaped velocity-position trajectory through k_v-k_z, as shown in Fig. 1. In this way, each voxel is imaged repeatedly as if with phase-contrast lobes of increasing size. A bipolar pulse is prepended to shift the trajectory about the origin, as shown in the grayed part of the waveform and trajectory in Fig. 1. Many of the acquired samples do not fall within the shaded region of interest (ROI) in *k*-space that is required to support the desired spatial and velocity resolution. These samples are not useful during image reconstruction.

The velocity FOV (or range) is computed by the inverse of the widest spoke spacing at the edge of the bowtie, and the spoke spacing is proportional to the distance in k_z that is covered by each lobe. In order to travel farther in k_v space, a longer distance in k_z must also be traversed. This implies that it is not possible to fix the number of samples or readout time and trade-off between velocity FOV and velocity resolution, as is done with normal position imaging. The challenge in sampling k_v-k_z is to cover a usable region quickly and efficiently given the constraints imposed by the gradients, and, more importantly, given the way the first moment accrues with time. When choosing the size of the bipolar readout lobes, one must make a trade-off between reaching the desired location in k_v quickly and selecting the number of desired samples in k_v based on the desired FOV and resolution.

Figure 2 illustrates this trade-off. For a given set of gradient hardware limits on the readout, the solid black line plots the furthest distance in k_v that can be reached with the minimum-length bipolar lobe. The minimum-length lobe is computed using gradient amplifier and coil limitations of maximum amplitude 40 mT/m and maximum slew rate of 150 T/m/s. Each successive line plots the furthest k_v that can be reached after the minimum-length uniform-density bipolar lobe pulse train of 1, 3, 5, 7, and 9 repetitions. The curves become spaced more closely together as more and more lobes are used. While the most efficient way to build a specified amount of first moment is to use a single bipolar waveform, the trajectory slope in k_v as a function of k_z increases linearly with time. Therefore, the speed of the velocity frequency does not remain constant, but increases linearly as a function of time. For example, the time required to build a given first moment

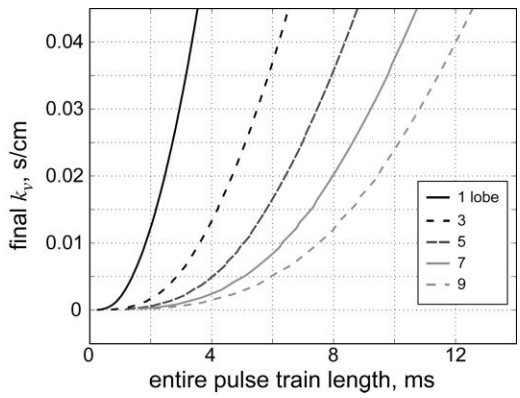

FIG. 2. An illustration of the farthest distance in k_v that can be reached with the minimum-length bipolar lobe, or the minimum-length train of uniform bipolar lobes. Because of the decreased spacing with longer pulse trains, variable-density sampling will give the largest speed increases for large flow velocities that necessitate relatively coarse velocity resolutions.

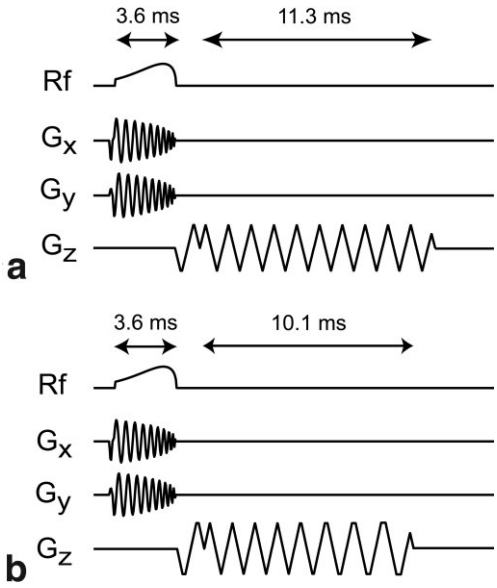

FIG. 3. Pulse sequence diagrams for the normal velocity range comparison: (**a**) uniform-density sequence and (**b**) variable-density sequence.

with two sequential bipolar waveforms will be less than twice the time required by a single bipolar waveform to achieve the same first moment. Therefore, it makes the most sense to use variable density for relatively short readout lengths (on the order of 10 ms) for large flow velocities that would otherwise necessitate the use of relatively coarse resolutions (on the order of 25–50 cm/s).

Another consequence of the first-moment accrual is that it is not possible to collect large k_v samples while moving through velocity k-space at the same speed during which low k_v samples are collected. The trajectory shape imposes a footprint that causes a significant variance in k_v sample density across k_z for steeply sloped spokes at large values of k_v. The result is a velocity FOV that varies with position along the excitation. This point is well discussed in Ref. 29.

MATERIALS AND METHODS

Pulse Sequences

Two uniform- and variable-density sequence comparisons were performed: one with a lower-velocity FOV to measure velocities in the normal ranges found in the ascending aorta, and one with a higher-velocity FOV to accommodate velocities in the range found in stenotic vessels and valves. The sequence diagrams for the normal-range comparison are shown in Fig. 3. The velocity parameters of the two versions of each sequence are summarized in Table 1.

All four sequences used a 3.6-ms, eight-turn spiral cylindrical excitation (23), with a measured full width at half maximum (FWHM) of 2 cm and a 17-cm sidelobe distance. The excitation was followed by a bipolar prewinding gradient that was 1.2–1.4 ms long (depending on the readout parameters) for the purpose of shifting the widest portion of the bowtie to the ROI in k_v-k_z. The bipolar-lobe pulse train readout gradients followed. The readout times were 11.3 ms and 10.1 ms for the normal-range uniform- and variable-density waveforms, respectively (the corresponding k_v-k_z trajectories are shown in the top half of Fig. 4). Since the velocity FOV is small enough (i.e., the k_v-spoke spacing is large enough) to necessitate a gradient that rises to peak amplitude, the variable-density bipolar lobe widths increase to widen the spoke-spacing at high values of k_v. In the high-FOV case, the readout times are 13.5 ms for the uniform-density version and 14.6 ms for the variable-density readout, resulting in the k_v-k_z trajectories shown in the bottom half of Fig. 4. Since the first few spokes about the origin must be more closely spaced to achieve a larger unaliased velocity FOV, the readout gradient amplitude starts below the gradient limits, and the bipolar lobe amplitudes increase to create the variable-density readout.

The uniform-density normal-range readout was designed to accommodate a normal aortic velocity FOV of 400 cm/s to observe velocities of $\pm$200 cm/s without aliasing with a velocity resolution of 33 cm/s. The corresponding variable-density readout was chosen for the same FOV, but with an improved resolution of 25 cm/s, using a density reduction factor (which we define as the factor by which the leading-edge spoke spacing is widened) of 2.75. The spatial FOV in both sequences was set according to the sensitivity of the coil used. A 5-inch coil was used for all experiments, and therefore the readout bandwidth was set for a spatial FOV of 12.7 cm, half of the available spatial FOV from sample spacing along the readout. The spatial resolution was 1.4 cm, and was chosen for the smallest voxel size at which ringing of the point spread function (PSF) remained below 20% of the peak signal. These parameters represented the finest velocity resolution possi-

Table 1
Parameter Values for Uniform- and Variable-Density One-Shot FVE Imaging

Sequence	Uniform-density, normal range	Variable-density, normal range	Uniform-density equivalent: improved resolution	Uniform-density, large FOV	Variable-density, large FOV	Uniform-density equivalent: larger FOV
Readout length (ms)	11.3	10.1	14.5	13.5	14.6	23.1
Velocity FOV (cm s^{-1})	400	400	400	525	1000	1000
Velocity resolution (cm s^{-1})	33	25	25	33	33	33
Density reduction factor	–	2.75	–	–	2.75	–
Number of spokes	11	9	14	14	16	28
No. of varying-density spokes	–	5	–	–	10	–
Fraction of k-space ROI acquired	0.6	0.6	0.6	0.65	0.6	0.65

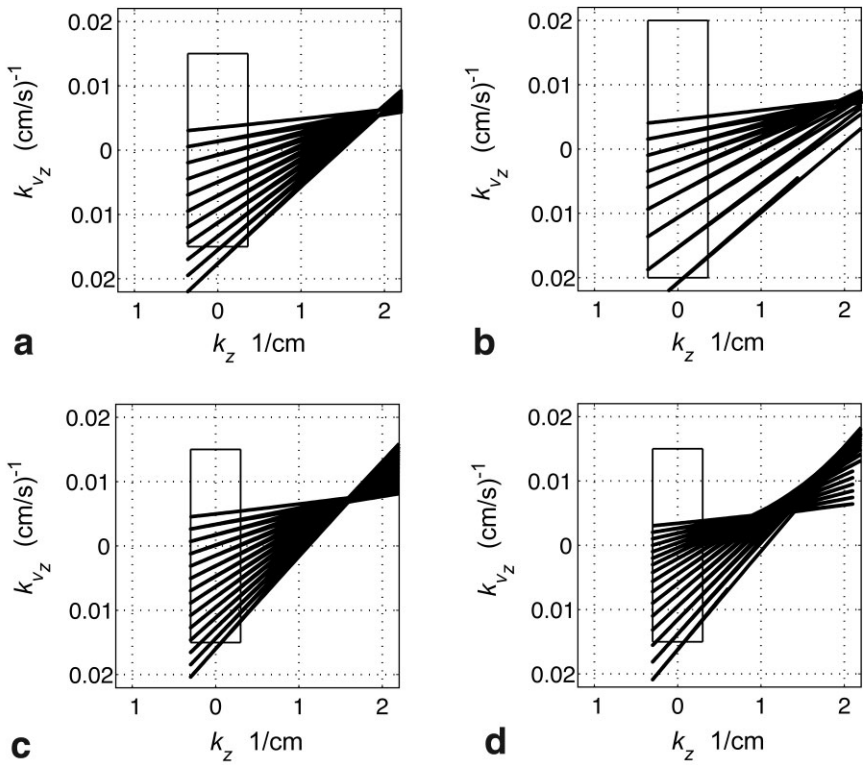

FIG. 4. Comparison of the four uniform- and variable-density trajectories. **a:** Uniform-density trajectory with 400 cm/s velocity FOV and 33 cm/s velocity resolution. **b:** Variable-density trajectory with same velocity FOV as part **a** and 25 cm/s velocity resolution. **c:** Uniform-density trajectory with 525 cm/s velocity FOV and 33 cm/s resolution. **d:** Variable-density version with the same velocity resolution and 1000 cm/s velocity FOV.

ble subject to the ringing constraint while maintaining a 400 cm/s FOV and a readout time of 11 ms to minimize temporal blurring of the velocity profile (29).

The large-FOV uniform- and variable-density sequences were designed to accommodate as large a velocity FOV as possible within a 15-ms readout time, at a velocity resolution of 33 cm/s. The uniform-density sequence had a velocity FOV of 525 cm/s, or ±262 cm/s. The variable-density version accommodated a 1000 cm/s FOV, or ±500 cm/s using the same density reduction factor of 2.75 to increase the spoke-spacing width. The spatial FOV along the excitation was 12.7 cm, with a spatial resolution of 1.7 cm. Note that the parameters for both the normal-range and large-FOV versions apply only under our given gradient limitations of 40 mT/m amplitude and 150 T/m/s slew rate.

Experimental Setup

All of the phantom and in vivo experiments were performed on a GE Signa 1.5 T scanner (GE Medical Systems, Milwaukee, WI, USA) with CV/i gradients. This system has a maximum gradient amplitude of 40 mT/m, maximum slew rate of 150 T/m/s, and a receiver sampling bandwidth of ±125 kHz. In both the phantom and patient scans, a body coil was used for RF transmission and a 5-inch surface coil was used for reception.

For each FVE measurement, a time series of velocity-position images were acquired. A single position along the vessel was chosen from which the velocity spectrum at that position was displayed as a velocity-time image with a window of 5 s. Each time frame was reconstructed by the following procedure: First, frequency samples were selected in the *k*-space ROI along only left–right-moving spokes, so that no eddy-current phase correction was necessary (29). The selected ROI samples were then density-compensated and resampled to a Cartesian uniform distribution using the Kaiser-Bessel gridding kernel of Jackson et al. (32). Finally, the gridded data were passed to a homodyne reconstruction using the FFT (33). The peak velocity was read from each velocity-time image after zero-padding by a factor of 4. The highest recorded velocity was the highest velocity in the waveform with a signal magnitude of above 20% of the peak signal magnitude of the velocity-position image. This threshold was chosen in accordance with the constraint placed on the acceptable level of Gibbs ringing.

Simulations

We determined that the acceptable amount of Gibbs ringing would limit design choices in the trade-off between temporal resolution and velocity FOV/resolution. For each trajectory, we first performed simulations to find that trajectory's PSF. A data vector containing ones at each bowtie sample was passed to the reconstruction to simulate an impulse signal with perfect gradients, without the presence of off-resonance. This simulation was used to select the final design parameters of velocity resolution, spatial resolution, and partial *k*-space fraction for the uniform-density trajectories, as well as the density reduction factor for the variable-density trajectories for a given desired velocity FOV. The parameters were chosen to achieve the highest velocity resolution subject to the constraint that any ringing was kept below 20% of the peak signal.

A second set of simulations was performed to compare simulated data from zero velocity at all positions with images along the flow phantom tube with the pump off.

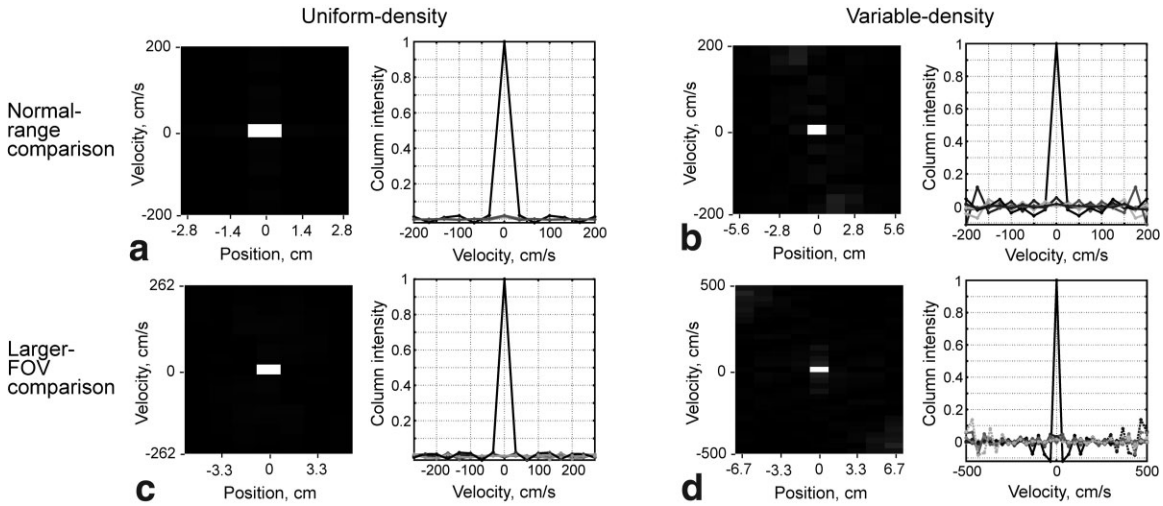

FIG. 5. PSF simulations of each trajectory: velocity-position images. **a:** Normal-range uniform-density sequence with 33 cm/s velocity resolution. **b:** Normal-range variable-density sequence with 25 cm/s velocity resolution. **c:** Large-FOV uniform-density sequence with 33 cm/s velocity resolution. **d:** Large-FOV variable-density sequence with 33 cm/s velocity resolution. The ringing shown in each PSF image is at or below 20% of the peak signal at the zero velocity/position location.

For all four trajectories, the above method was used to simulate data with the pump off, except that only samples along the k_v axis were set to one. We did this to compare the ringing from sampling the corresponding *k*-space locations with images acquired in the flow phantom with the pump turned off.

Phantom Experiments

To simulate normal ascending aortic flow, phantom experiments were performed with Tygon R-3603 tubing (1.75 cm inner diameter) connected to a pulsatile blood pump for dogs/monkeys (model 1421; Harvard Apparatus, Holliston, MA). To check consistency in the peak flow rate measured by the uniform- and variable-density sequences, the flow rate on the pump was varied between the marked settings of 15, 20, 25, and 30 cm^3/stroke, the maximum pump flow rate setting. The pumping frequency, which could also be controlled, was set to 40 cycles/min for the tube experiments, in order to maximize the number of frames obtained in one phase of the pump cycle. To simulate a jet with disturbed flow patterns, we created a stenosis phantom by placing an 3-cm graduated connector (end diameter = 1.6 mm) into a cross section of the 1.75-cm diameter tubing to create a jet of fast flow with disturbed flow inside the tube and outside the graduated piece. In addition, the pump rate was increased to 60 and 80 cycles/min, the maximum pump frequency at which the tubing connectors functioned reliably, while the flow rate was kept at the maximum setting of 30 cm^3/stroke. The pump rate was increased to match heart rates expected in patients with aortic stenosis, as well as to maximize the velocity that could be achieved in the phantom with the pump. Both phantoms were first scanned using an existing real-time imaging system (34,35). A real-time interactive sequence was used to center the excitation beam along the tube or stenosis phantom. We expect that off-resonance may cause some blurring and shifting of the velocity spectrum. To simulate the effects of off-resonance, the study in the 1.75-cm tube flow phantom was repeated with the scanner modulation frequency offset by 100 Hz and 200 Hz.

Each of the four trajectories was measured on the gradient hardware using the method of Gurney et al. (36), which extends the work of Duyn et al. (37). During reconstruction, the tube phantom images were gridded to both the designed and measured trajectories for evaluation. In addition, the same method also provided measurements of the B_0 eddy currents on each of the three gradient axes. The flow phantom tube was positioned along the *Z*-axis to allow B_0 eddy currents to be corrected during image reconstruction. After eddy-current correction was performed along the *Z*-axis, the measured eddy currents on the *X*- and *Y*-gradient axes were applied to the reconstructed images to demonstrate the effects of each.

In Vivo Experiments

In vivo images were acquired in the ascending aorta of normal volunteers, with the excitation positioned in alignment with the vessel. All subjects gave informed consent in accordance with Stanford University policy after they were screened for possible MRI risk factors. The same real-time interactive sequence as used in the flow phantom experiments was used to localize the ascending aorta of each subject just above the aortic valve. One subject was taken to the Noninvasive Cardiovascular Imaging Laboratory at Stanford Hospital and Clinics prior to the scan, and examined with Doppler US for peak velocity comparison with FVE.

RESULTS

Simulations

A simulation of the PSF of each trajectory was first performed to verify the parameter choices. Figure 5 shows the

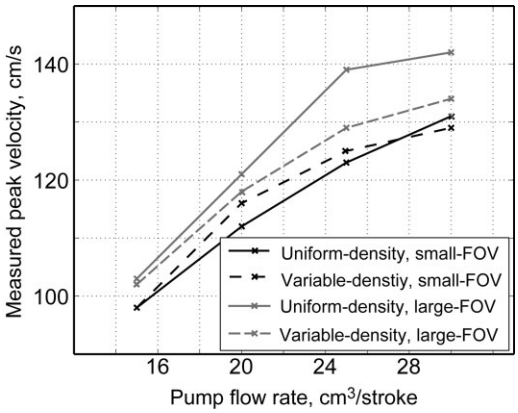

FIG. 6. Plot of measured velocities vs. pump flow rate in the tube phantom fed by a pulsatile pump, at four pump settings. The peak velocity, the highest velocity in the waveform with signal above 20% of the peak image signal, is read from velocity-time images (k_v-space zero-padded to the same size). The measurements are consistent within velocity voxel sizes.

velocity-position PSF of each of the four sequences. In both uniform-density sequences, Gibbs ringing is below 10% of the maximum signal level and is nearly undetectable at the final design parameters chosen. The variable-density versions have aliasing artifact at the edges of velocity FOV, but this artifact is below 20% of the maximum signal level, an amount that can be easily display-windowed without degrading the visibility of the velocity spectra. When simulations were repeated with all z locations set to zero velocity to produce a k-space that was one along the k_v axis, the trajectory-sampled simulated images agreed well with images acquired in the tube flow phantom with the pump turned off.

Finally, PSF simulations were performed to determine the uniform-density parameters needed to measure the same velocity FOV or resolution as the variable-density version. These parameters are listed in the third and final columns of Table 1. In order to match the velocity resolution of the normal-range variable-density sequence, the uniform-density sequence must have a readout time increased by 32%. To increase the larger-range FOV from 525 cm/s to 1000 cm/s, the number of spokes would have to be doubled to 28, with a corresponding readout duration of over 23 ms (71% longer than the uniform-density sequence with an FOV of 525 cm/s).

Flow Phantom Experiments

Normal Aortic-Velocity Range

Results from flow studies in the 1.75-cm tube fed by the pulsatile pump at a range of velocities that simulated the range of normal aortic flow are plotted in Fig. 6. Measurements using the different trajectories were consistent within velocity-resolution widths of 25 and 33 cm/s. Velocity-time images from each of the four sequences are shown in Fig. 7. The images show 5 s of data at the center position of the excitation with the pump set to a rate of 20 cm^3/stroke. The top two images show the finer resolution (25 cm/s vs. 33 cm/s) that can be achieved in a slightly shorter readout time. The bottom images show how variable density can be used to increase the velocity FOV significantly. Minimal aliasing artifact from the undersampling of high-velocity frequencies is observed.

When the actual k-space trajectory was measured using the technique described in Ref. 36, the maximum sample shift in k_v was 1% of the maximum extent of k_v covered by the trajectory. When images were reconstructed after flow phantom data samples were gridded to both trajectories, there was no perceptible difference in the velocity-position images. The maximum B_0 eddy currents were below 8° on the X- and Z-gradient axes, and at or below 15° on the Y-gradient axis. Correction of the Z-gradient eddy currents made no perceptible difference for reconstruction of the flow phantom images, nor did addition of the Y-gradient eddy-current errors to simulate the worst case.

Off-Resonance Simulations

Figure 8 shows the off-resonance simulation results obtained with the two uniform-density versions of the sequence. Images from both of the uniform-density versions without the presence of off-resonance are provided on the left (a and d) for comparison. Images b and e result when 100 Hz of off-resonance is simulated with both sequences, and images c and f result from the simulation of 200 Hz of off-resonance. The shift of the waveform in the velocity direction is that of one velocity voxel per 100 Hz, which is what is expected with a 10-ms readout. Figure 9 shows the results of the same simulation with the two variable-density versions of the sequence: images without off-resonance, those with 100 Hz, and those with 200 Hz of off-resonance. A larger shift of 1–2 velocity voxels per 100 Hz of off-resonance is observed in the velocity direction. There is also some loss of low-signal velocities below the peak velocity due to blurring of the velocity spectra.

Stenotic Velocity Range

Velocity-time images in the stenosis phantom are shown in Fig. 10. The figure gives a comparison of 5 s of data for all four sequences. The comparison of the four sequences at maximum flow rate (30 cm^3/stroke) and pump frequency of 60 cycles/min are shown on the left. The normal-range sequences make it difficult to measure peak velocity; however, the aliased velocity can be read off of the larger-FOV uniform-density image. This sequence gives an unwrapped peak velocity of 478 cm/s. The larger-FOV variable-density sequence, which does not alias the velocity spectrum, gives a peak velocity measurement of 467 cm/s. Images to compare measurements of the velocity spectra with the pump rate kept at the maximum of 30 cm^3/stroke and pump frequency set to 80 cycles/min are shown on the right of Fig. 11. Unwrapping the velocity aliasing in the larger-FOV uniform-density image gives a peak velocity measurement of 416 cm/s. The peak velocity measured by the variable-density version of the sequence is 379 cm/s, and no unwrapping of the velocity spectrum is necessary.

In Vivo Experiments

Three healthy volunteers were scanned with three of the four sequences: the two normal-range FOV uniform- and

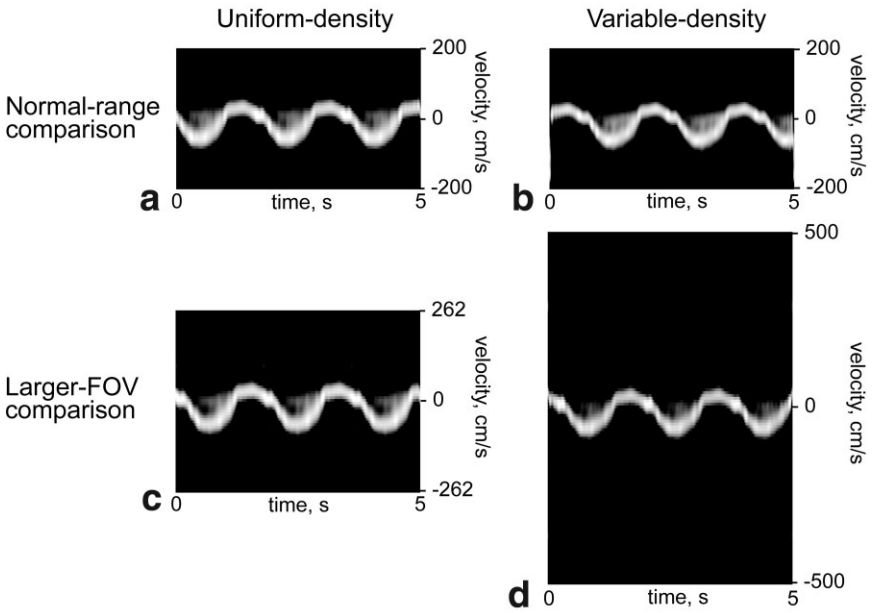

FIG. 7. Velocity-time images in a tube phantom fed by a pulsatile pump, at a pump rate of 40 cycles/min and flow rate of 20 cm^3/stroke. **a** and **b:** The top two images demonstrate an improvement in velocity resolution from 33 cm/s to 25 cm/s using variable-density sampling. **c** and **d:** The bottom two images show the factor of 2 improvement that is possible when variable-density sampling is used to increase the velocity FOV, which allows the measurement of jet velocities without aliasing.

variable-density versions, and the large-FOV variable-density sequence. In each volunteer, the ascending aorta was first localized using the real-time spiral sequence. One of the subjects was also examined using Doppler US for comparison with the three FVE sequences. Images from the echo and MR studies in this subject are shown in Fig. 11. The US study measured peak flow to be 120 cm/s. The uniform-density sequence measured peak flow to be 123 cm/s, and the variable-density higher-resolution version measured peak flow to be 106 cm/s. The high-FOV variable-density sequence measured the subject's peak flow to be 129 cm/s.

DISCUSSION

The PSF simulations demonstrated that the amount of Gibbs ringing can be used as a metric by which the design parameters can be adjusted given a desired velocity FOV and resolution. Specifically, trade-offs must be made between minimizing readout time, minimizing aliasing artifact from high (undersampled) frequencies, and improving velocity FOV and resolution. With respect to the readout time, adjustments must often be made in coarse intervals. Since the gradient waveform is currently at gradient hardware and amplifier limits, often another spoke must be added to the bowtie trajectory to increase k_v sampling. This necessitates an increase in readout time equal to the length of a full bipolar lobe for a FOV increase, or a partial bipolar lobe for an increase in resolution (since the last spoke can be cut short to the right edge of the spatial FOV.)

A second consequence relates to the relative gains achieved by using variable-density sampling to increase either velocity FOV or resolution. The PSF simulations demonstrated that there is a greater cost in readout time to increase the velocity FOV of a uniform-density sequence than to increase the velocity resolution, while maintaining

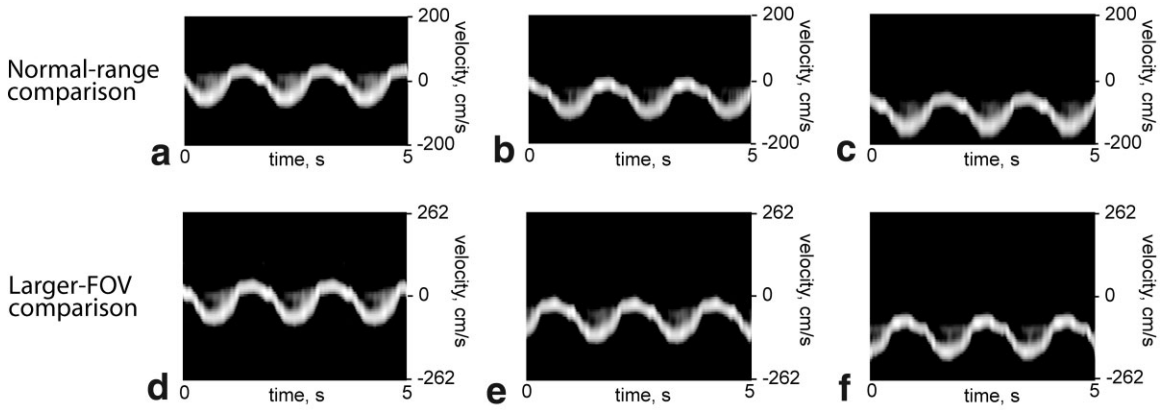

FIG. 8. Off-resonance velocity-time image comparisons for the uniform-density versions. **a–c:** Normal-range sequence with (**a**) zero frequency offset for comparison, (**b**) 100 Hz offset, and (**c**) 200 Hz offset. **d–f:** High-velocity FOV sequence with (**d**) zero frequency offset, (**e**) 100 Hz offset, and (**f**) 200 Hz offset. The primary effect of off-resonance is a shift of one velocity-voxel per 100 Hz of off-resonance, as is expected with a 10-ms readout.

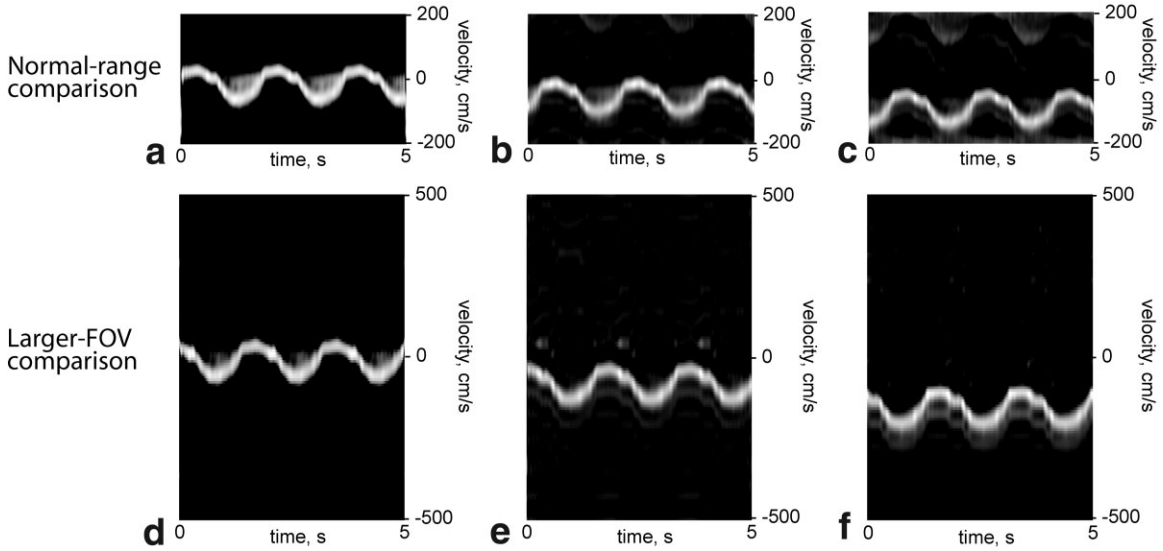

FIG. 9. Off-resonance velocity-time image comparisons for the variable-density versions. **a–c:** Normal-range sequence with (**a**) zero frequency offset for comparison, (**b**) 100 Hz offset, and (**c**) 200 Hz offset. **d–f:** High-velocity FOV sequence with (**d**) zero frequency offset, (**e**) 100 Hz offset, and (**f**) 200 Hz offset. The shift in the spectra due to off-resonance is 1–2 voxel sizes for every 100 Hz, as is expected with a 14-ms readout. Blurring of the spectra also results in some loss of signal from the velocities that account for a smaller proportion of the spectra.

acceptable ringing levels. Therefore, a larger gain can be achieved by using variable-density sampling to increase the velocity FOV. This agrees with the results obtained after the farthest k_v's reached for different bipolar trains were plotted (Fig. 2), and indicates that variable-density sampling will make the most sense for large flow velocities.

A higher gradient amplitude and slew rate, if available, will result in shorter lobe lengths. Due to the higher time dependence on the first moment, increases in amplitude and slew have different effects on the bipolar lobe length, depending on the desired incremental change in k_v. For a single bipolar lobe, an increase in slew rate alone offers the largest decrease in lobe length at the lowest velocity frequencies. For a fixed slew-rate increase, the amount of lobe shortening decreases exponentially with increasing Δk_v. Increases in gradient amplitude, however, result in no lobe shortening for low k_v values, with increasing shortening as Δk_v increases. For gradients stronger than 40 mT/m at 150 T/m/s slew, there is no advantage with higher-amplitude gradients for velocity readouts that measure spectra with velocity-FOV above 250 cm/s ($\pm$125 cm/s), since below the corresponding Δk_v of 0.004 s/cm, bipolar lobes are not amplitude-limited. Increasing the gradient amplitude does shorten the bipolar lobes used in FVE, provided the slew rate is also increased. For the four *k*-space trajectories discussed in this paper, doubling the slew rate alone results in a decrease in readout time of 13–27%. A simultaneous doubling of both the slew rate and gradient amplitude results in a readout time decrease of 21–28%.

Our simulations demonstrate that the velocity spectrum is shifted in the presence of off-resonance. In both of the normal-range sequences, our simulations indicated that the shift was equal to one velocity voxel width for every 100 Hz of off-resonance. In both of the larger-FOV sequences, the shift due to off-resonance was 1–2 velocity voxel widths per 100 Hz. This agrees well with our expectations, since readouts are 10 ms and 14 ms for the normal-range and large-FOV sequences, respectively. We would thus expect a shift of one velocity voxel per 100 Hz for the normal-range sequences, and a shift of one voxel per 70 Hz for the larger-FOV sequences. For a small amount of off-resonance, it is possible to correct the shift based on the baseline flow at $v = 0$.

One concern that arises with the use of variable-density FVE is that it blurs the velocity spectrum. Since the off-resonance results in a linear phase as a function of k_v, the uniform-density FVE is not blurred in the presence of off-resonance—it is only shifted (29). When variable-density sampling is applied to FVE, a weighting is given to the spokes such that the k_v values that are more sparsely sampled are emphasized. Specifically, the more sparsely-sampled spokes are given extra emphasis after the density correction weighting performed during gridding is computed. If these sparser samples are not emphasized to avoid falloff of density in k_v, and are only corrected along k_z, the data will reconstruct an image that has been low-pass filtered. This emphasis results in a linear weighting in k_v, which causes the off-resonance linear phase in k_v to appear as a higher-order quadratic term. This resulting quadratic phase tends to blur the velocity spectra. According to the tests in the flow-phantom with spatially invariant off-resonance, the peak velocity measurement is not affected by this blurring, but velocities of fewer spins with lower signal are lost in windowing. To keep the shift from off-resonance below a single k_v-voxel, two shorter readouts could be interleaved to achieve similar acquired trajectories, with a slight increase in temporal averaging but shorter readouts (38).

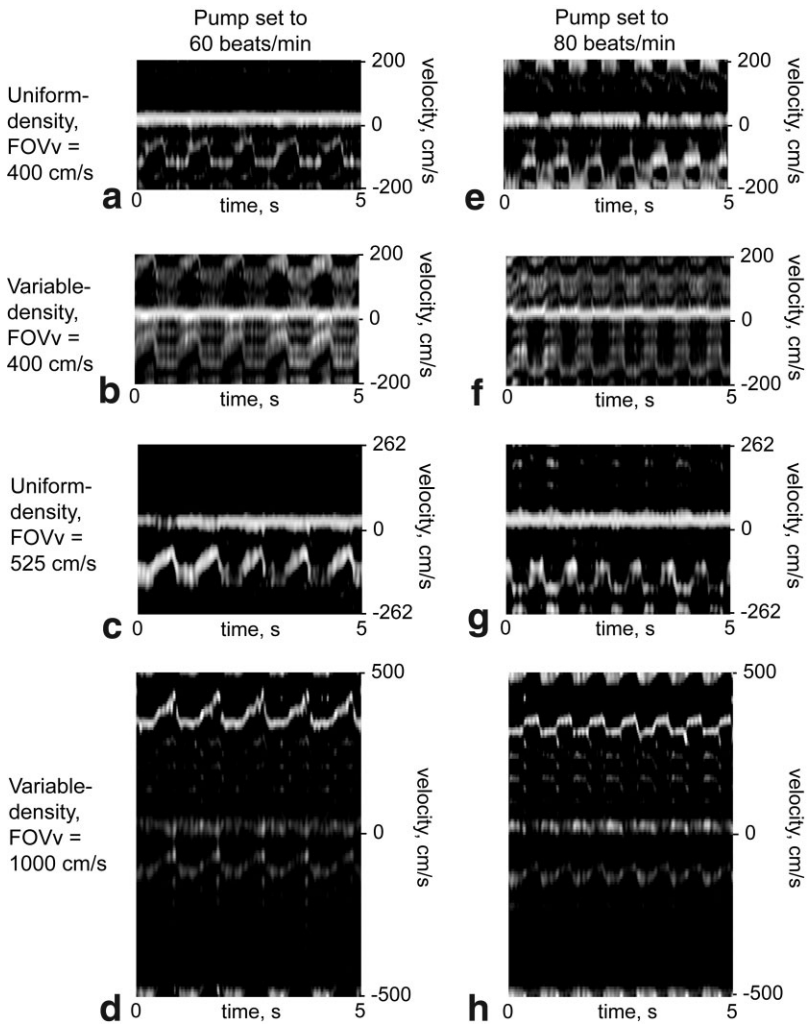

FIG. 10. Velocity-time images in the stenosis phantom fed by a pulsatile pump, illustrating a velocity FOV that is large enough to unambiguously detect jets, which is the largest gain from the application of variable-density sampling to FVE. Pump set to maximum flow rate of 30 cm^3/stroke at two rates ((**a–d**) 60 cycles/min and (**e–h**) 80 cycles/min) to image the peak velocities that could be created in the stenosis phantom. **a** and **e:** Uniform-density normal-range FVE. **b** and **f:** Variable-density normal-range FVE, showing significant ambiguity due to the degree of velocity aliasing. **c** and **g:** Uniform-density large-FOV FVE. Unwrapping the images results in peak velocities of 478 cm/s for the pump rate of 60 cycles/min, and 416 cm/s for the pump rate of 80 cycles/min. **d** and **h:** Variable-density large-FOV FVE. The velocity spectra are unaliased, with peak velocity measurements of 467 cm/s at a pump rate of 60 cycles/min, and 379 cm/s at a pump rate of 80 cycles/min. All of the images were windowed; however, smaller-FOV images were windowed to a lesser degree because the wraparound diminished the signal difference between the spectra and the aliasing artifact.

When the stenosis flow phantom was imaged, velocities at the output of the stenosis phantom were expected to increase by a factor of 3–4 times that in the tube without the stenosis phantom. The change of shape in the velocity-time images at the higher pump rates makes it difficult to determine whether the flow was aliased, which would cause significant ambiguity when trying to measure flow in a patient with suspected aortic stenosis using the normal-range or larger-FOV uniform-density sequences. The variable-density large-FOV sequence, however, was able to capture the velocity spectrum without aliasing. Since the peak velocities measured by the variable-density large-FOV sequence agreed well with the unwrapped uniform-density large-FOV measurements, we conclude that using variable-density sampling to increase the velocity FOV for detection of jets can help one obtain an unambiguous measurement.

The peak velocity measurements obtained in a normal volunteer by variable-density FVE agreed well with those measured using Doppler US. In addition, the normal-range variable-density sequence gave a much sharper velocity spectrum when compared with the normal-range uniform-density version. This suggests that although the gain achieved by using variable-density to improve velocity resolution is less dramatic than the gain achieved by using it to improve velocity FOV, it is worthwhile for normal-range velocity measurement. The result of the larger-FOV measurement proved quite promising. In both the normal-range and larger-FOV variable-density sequences, aliasing artifact was minimal and easily windowed without any loss of peak velocity information.

CONCLUSIONS

We have described the use of variable-density sampling for 1D FVE, and presented comparisons with uniform-density FVE and Doppler US. By modifying a uniform-density FVE sequence with a velocity FOV of 400 cm/s to use variable density, we demonstrated an improvement of velocity resolution from 33 cm/s to 25 cm/s. The PSF simulations indicate that to achieve this resolution using the uniform-density sequence, the readout time would have to be increased by 31%. By modifying a uniform-density sequence with a velocity FOV of 525 cm/s to use variable density, we demonstrated an increase in velocity FOV to 1000 cm/s, an increase that would require a 71% increase in readout time. Variable-density sampling can be used to shorten the readout time or improve the velocity resolution of 1D FVE, but its main advantage is its ability to image peak flow velocities in regions of stenosis without

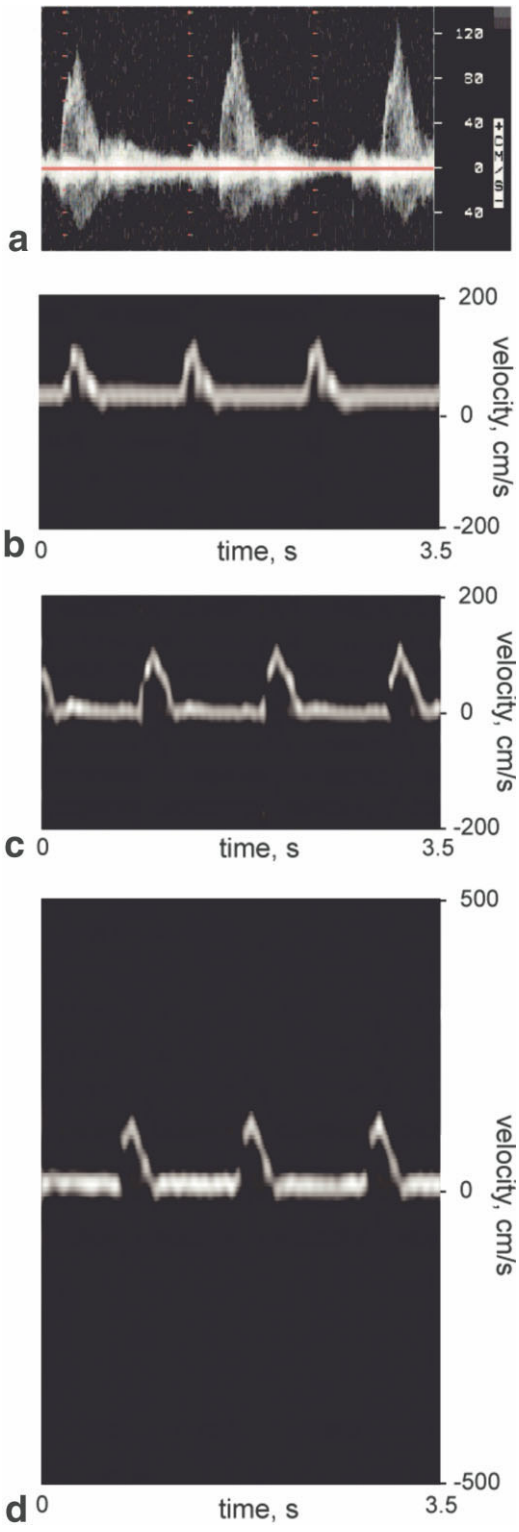

FIG. 11. Velocity-time images showing excellent agreement between the FVE measured peak velocity and Doppler US. Images were acquired in the ascending aorta of the same normal volunteer with an average heart rate of 60 beats/min. **a:** Doppler US image, with a peak velocity of 120 cm/s. **b:** Image using normal-range uniform-density FVE, with a peak velocity of 123 cm/s. **c:** Image using normal-range variable-density FVE, with improved velocity resolution and a peak velocity of 106 cm/s. **d:** Image using large-FOV variable-density FVE, with a peak velocity of 129 cm/s. The FOV is increased to 1000 cm/s with minimal aliasing artifact. The FVE images were windowed, such that aliasing artifacts are barely visible.

aliasing. In areas of highly pulsatile and stenotic flow, real-time imaging with high temporal, spatial, and velocity resolution is essential. Studies in phantoms and healthy volunteers confirm that variable-density acquisition of k_z-k_v substantially improves the velocity and temporal resolution of such data. Further evaluations in patients with aortic and valvular stenoses are needed to establish this as a clinical tool.

ACKNOWLEDGMENTS

We thank Christopher Macgowan and Jeffrey DiCarlo for helpful discussions and the National Science Foundation for fellowship support.

REFERENCES

1. Robson DJ, Flaxman JC. Measurement of the end-diastolic pressure gradient and mitral valve area in mitral stenosis by Doppler ultrasound. Eur Heart J 1984;5:660–667.
2. Tei C, Kisanuki A, Arikawa K, Otsuji Y, Arima S, Kashima T, Tanaka H, Kushitani M, Shah PM. [Continuous wave Doppler echocardiographic assessment of aortic stenosis and aortic regurgitation]. J Cardiogr 1985; 15:111–121.
3. Nishimura RA, Rihal CS, Tajik AJ, Holmes Jr DR. Accurate measurement of the transmitral gradient in patients with mitral stenosis: a simultaneous catheterization and Doppler echocardiographic study. J Am Coll Cardiol 1994;24:152–158.
4. Meyer JI, Khalil RM, Obuchowski NA, Baus LK. Common carotid artery: variability of Doppler US velocity measurements. Radiology 1997;204:339–341.
5. Logason K, Barlin T, Jonsson ML, Bostrom A, Hardemark HG, Karacagil S. The importance of Doppler angle of insonation on differentiation between 50–69% and 70–99% carotid artery stenosis. Eur J Vasc Endovasc Surg 2001;21:311–313.
6. Steel R, Ramnarine KV, Davidson F, Fish PJ, Hoskins PR. Angle-independent estimation of maximum velocity through stenoses using vector Doppler ultrasound. Ultrasound Med Biol 2003;29:575–584.
7. Flamm SD, Muthupillai R. Coronary artery magnetic resonance angiography. J Magn Reson Imaging 2004;19:686–709.
8. Pujadas S, Reddy GP, Weber O, Lee JJ, Higgins CB. MR imaging assessment of cardiac function. J Magn Reson Imaging 2004;19:789–799.
9. Kilner PJ, Firmin DN, Rees RS, Martinez J, Pennell DJ, Mohiaddin RH, Underwood SR, Longmore DB. Valve and great vessel stenosis: assessment with MR jet velocity mapping. Radiology 1991;178:229–235.
10. Kilner PJ, Manzara CC, Mohiaddin RH, Pennell DJ, Sutton MG, Firmin DN, Underwood SR, Longmore DB. Magnetic resonance jet velocity mapping in mitral and aortic valve stenosis. Circulation 1993;87:1239–1248.
11. Eichenberger AC, Jenni R, von Schulthess GK. Aortic valve pressure gradients in patients with aortic valve stenosis: quantification with velocity-encoded cine MR imaging. AJR Am J Roentgenol 1993;160: 971–977.
12. Sondergaard L, Hildebrandt P, Lindvig K, Thomsen C, Stahlberg F, Kassis E, Henriksen O. Valve area and cardiac output in aortic stenosis: quantification by magnetic resonance velocity mapping. Am Heart J 1993;126:1156–1164.
13. Sondergaard L, Stahlberg F, Thomsen C, Stensgaard A, Lindvig K, Henriksen O. Accuracy and precision of MR velocity mapping in measurement of stenotic cross-sectional area, flow rate, and pressure gradient. J Magn Reson Imaging 1993;3:433–437.
14. Pike GB, Meyer CH, Brosnan TJ, Pelc NJ. Magnetic resonance velocity imaging using a fast spiral phase contrast sequence. Magn Reson Med 1994;32:476–483.
15. Gatehouse PD, Firmin DN, Collins S, Longmore DB. Real time blood flow imaging by spiral scan phase velocity mapping. Magn Reson Med 1994;31:504–512.
16. Debatin JF, Leung DA, Wildermuth S, Botnar R, Felblinger J, McKinnon GC. Flow quantitation with echo-planar phase-contrast velocity mapping: in vitro and in vivo evaluation. J Magn Reson Imaging 1995; 5:656–662.

17. Nayak KS, Pauly JM, Kerr AB, Hu BS, Nishimura DG. Real-time color flow MRI. Magn Reson Med 2000;43:251–258.
18. Nayak KS, Hu BS, Nishimura DG. Rapid quantitation of high-speed flow jets. Magn Reson Med 2003;50:366–372.
19. McKinnon GC, Debatin JF, Wetter DR, von Schulthess GK. Interleaved echo planar flow quantitation. Magn Reson Med 1994;32:263–267.
20. Moran PR. A flow velocity zeugmatographic interlace for NMR imaging in humans. Magn Reson Imaging 1982;1:197–203.
21. Bittoun J, Bourroul E, Jolivet O, Idy-Peretti I, Mousseaux E, Tardivon A, Peronneau P. High-precision MR velocity mapping by 3D-Fourier phase encoding with a small number of encoding steps. Magn Reson Med 1993;29:674–680.
22. Bittoun J, Jolivet O, Herment A, Itti E, Durand E, Mousseaux E, Tasu JP. Multidimensional MR mapping of multiple components of velocity and acceleration by Fourier phase encoding with a small number of encoding steps. Magn Reson Med 2000;44:723–730.
23. Pauly JM, Nishimura DG, Macovski A. A k-space analysis of small-tip-angle excitation. J Magn Reson 1989;81:43–56.
24. Schroder C, Bornert P, Aldefeld B. Spatial excitation using variable-density spiral trajectories. J Magn Reson Imaging 2003;18:136–141.
25. Dumoulin CL, Souza SP, Hardy CJ, Ash SA. Quantitative measurement of blood flow using cylindrically localized Fourier velocity encoding. Magn Reson Med 1991;21:242–250.
26. Hu BS, Pauly JM, Nishimura DG. Localized real-time velocity spectra determination. Magn Reson Med 1993;30:393–398.
27. Irarrazabal P, Hu BS, Pauly JM, Nishimura DG. Spatially resolved and localized real-time velocity distribution. Magn Reson Med 1993;30: 207–212.
28. Hardy CJ, Bolster Jr BD, McVeigh ER, Iben IE, Zerhouni EA. Pencil excitation with interleaved fourier velocity encoding: NMR measurement of aortic distensibility. Magn Reson Med 1996;35:814–819.
29. Pat GT, Pauly JM, Hu BS, Nishimura DG. One-shot spatially resolved velocity imaging. Magn Reson Med 1998;40:603–613.
30. Tsai CM, Nishimura DG. Reduced aliasing artifacts using variable-density k-space sampling trajectories. Magn Reson Med 2000;43:452–458.
31. Sabataitis JC, Luk-Pat GT, Hu BS, Nishimura DG. One-shot Fourier velocity-encoding using a variable-density trajectory. In: Proceedings of the 9th Annual Meeting of ISMRM, Glasgow, Scotland, 2001. p 372.
32. Jackson JI, Meyer CH, Nishimura DG, Macovski A. Selection of a convolution function for Fourier inversion using gridding (computerised tomography application). IEEE Trans Med Imaging 1991;10:473–478.
33. Noll DC, Nishimura DG, Macovski A. Homodyne detection in magnetic resonance imaging. IEEE Trans Med Imaging 1991;10:154–163.
34. Kerr AB, Pauly JM, Hu BS, Li KC, Hardy CJ, Meyer CH, Macovski A, Nishimura DG. Real-time interactive MRI on a conventional scanner. Magn Reson Med 1997;38:355–367.
35. DiCarlo JC, Hu BS, Nishimura DG, Pauly JM. One-shot Fourier velocity-encoding integrated with a real-time imaging system. In: Proceedings of the 10th Annual Meeting of ISMRM, Honolulu, 2002. p 1801.
36. Gurney P, Pauly JM, Nishimura DG. A simple method for measuring B_0 eddy currents. In: Proceedings of the 13th Annual Meeting of ISMRM, Miami, 2005. p 866.
37. Duyn JH, Yang Y, Frank JA, van der Veen JW. Simple correction method for k-space trajectory deviations in MRI. J Magn Reson 1998; 132:150–153.
38. DiCarlo JC, Hu BS, Nishimura DG, Pauly JM. Interleaved variable-density 1D Fourier velocity-encoding. In: Proceedings of the 11th Annual Meeting of ISMRM, Toronto, Canada, 2003. p 2507.